Modulation of the magnetic properties of gold-spinel ferrites heterostructured nanocrystals

Elvira Fantechi[1]*, Claudia Innocenti[2,3], Giovanni Bertoni[4,5], Claudio Sangregorio[2,3], Francesco Pineider[1]

[1] University of Pisa, Italy; [2] ICCOM-CNR, Sesto Fiorentino, Italy; [3] University of Florence, Italy; [4] IMEM-CNR, Parma, Italy; [5] CNR-NANO, Modena, Italy

We present the synthesis and the structural, magnetic and optical characterization of heterostructured nanocrystals based on Au and MFe_2O_4 (M=Fe, Co, Mn). We demonstrate the possibility to tune the magnetic properties of these nanostructures while keeping an excellent plasmonic response.

Nano Research

ISSN 1998-0124 CN 11-5974/O4
https://doi.org/(automatically inserted by the publisher)

Research Article

Modulation of the magnetic properties of gold-spinel ferrite heterostructured nanocrystals

Elvira Fantechi[1](✉), Claudia Innocenti[2,3], Giovanni Bertoni[4,5], Claudio Sangregorio[2,3], Francesco Pineider[1]

[1] *INSTM and Dept. of Chemistry and Industrial Chemistry, University of Pisa, Pisa 56124, Italy*
[2] *ICCOM-CNR, Institute for the Chemistry of OrganoMetallic Compounds, Sesto Fiorentino 50019, Italy*
[3] *INSTM and Dept. of Chemistry "U. Schiff", University of Florence, Sesto Fiorentino 50109, Italy*
[4] *IMEM-CNR, Institute of Materials for Electronics and Magnetism, Parma 43124, Italy*
[5] *CNR-NANO, Istituto Nanoscienze, Modena 41125, Italy*

Received: day month year / **Revised:** day month year / **Accepted:** day month year (automatically inserted by the publisher)

ABSTRACT

The rational design of complex nanostructures is of paramount importance to gain control over their chemical and physical properties. Recently, magnetic-plasmonic heterostructured nanocrystals have been recognized as key players in nanomedicine as multifunctional therapeutic-diagnostic tools and in catalysis. Here we show how the properties of gold-iron oxide heterostructured nanocrystals can be tuned by chemical doping of the magnetic subunit. The divalent cations in the iron oxide were substituted with cobalt and manganese to obtain a general formula Au-MFe_2O_4 (M = Fe, Co, Mn). Magnetic properties of the heterostructures could be tuned, while maintaining well-defined plasmon resonance signatures, confirming the dual magnetic-plasmonic functional capability of these nanostructures.

KEYWORDS

Heterostructured nanocrystals, seeded-growth, spinel ferrites, magnetic-plasmonic nanoparticles

1. Introduction

The significant progresses in the colloidal synthesis of inorganic nanocrystals (NCs) during these last decades opened the path to the preparation of complex colloidal nanostructures with a fine control on the mean size and chemical composition. In particular, significant momentum has been brought by recent exciting advances in the synthesis of heterostructured nanocrystals (HNCs) [1,2], in which two or more inorganic materials are combined at the nanoscale. This novel class of nanomaterials offers great opportunities towards the realization of complex multifunctional nanoplatforms for a wide range of applications, thanks to the combined action of the two functionalities or to the onset of new properties arising from the direct interaction of the two inorganic domains. Recently, significant efforts have been devoted to the realization of magnetic-plasmonic HNCs, in particular those based on gold (Au) and magnetite (Fe_3O_4). The extremely high interest towards these systems was mainly driven by the large potential in the biomedical field: indeed, both Au and Fe_3O_4 NCs can be employed as contrast agents for different imaging techniques (Magnetic Resonance Imaging (MRI) [3], X-Ray Computed Tomography (CT) [4,5], Photoacoustic imaging, among others [5]), heat mediators for antitumoral thermal therapies (magnetic hyperthermia [3] and photothermal therapy [5]) and as building blocks for the realization of biocompatible active nanoplatforms for delivery, targeting and sensing applications [3,5]. Within this framework, the combination of Au and Fe_3O_4 in a single nanosystem offers the possibility not only to strongly increase their functionality, but also to employ them in different modalities [6,7]. This concept is particularly interesting in the field of imaging: the integration of two or more different techniques allows overcoming the intrinsic limitations of the single ones and providing complementary information for a better diagnosis [6–8]. ~~The multimodal nature of~~ Au-Fe_3O_4 HNCs ha~~s~~ves ~~–~~ been demonstrated to act as efficient contrast agents for MRI alone [9–11] or in combination with epifluorescence/reflectance laser scanning confocal microscopy [12] and with X-ray-CT [13,14]~~. The contrast enhancement capability of Au-Fe_3O_4 HNCs in MRI was reported to be comparable to that observed for single Fe_3O_4 NCs of similar size [12,13] and very high values were found for Fe_3O_4 domains with octahedral shape [11]~~. The concept of multimodal approach can be applied also in the field of therapy, for example through the simultaneous application of two different hyperthermic techniques (as recently demonstrated by Espinosa *et al.* [15]) or through the design of drug-delivery nanoplatforms based on a different functionalization of the two counterparts.~~ The possibility to combine the effect of alternating magnetic field and irradiation with laser light was recently demonstrated by Espinosa *et al.* [15], who report a strongly enhanced hyperthermic efficiency of magnetic-plasmonic nanohybrids composed of Au and Fe_3O_4 with respect to the single techniques alone. C~~c~~oncerning Au-Fe_3O_4 HNCs, the investigation of their hyperthermic properties is still limited to the magnetic actuation, and high values of hyperthermic

Address correspondence to Elvira Fantechi, elvira.fantechi@dcci.unipi.it

efficiency have been recently reported [16]. On the other hand, interesting nanoplatforms based on Au-Fe_3O_4 HNCs have been developed, for example for a specific targeted drug-delivery approach against breast cancer ~~(through the functionalization of Fe_3O_4 domain with Herceptin and Au one with cis-platinum)~~ [17] or for the realization of dual responsive drug-delivery systems ~~(through the orthogonal functionalization with pH and temperature responsive polymers on the iron oxide and on the gold domain, respectively)~~.[18]

Besides biomedical applications, Au-Fe_3O_4 HNCs have demonstrated to act as promising catalysts for different chemical reactions ~~(CO oxidation~~ [19–25]~~, reduction of hydrogen peroxide [24] and nitrophenols [24], oxygen evolution reaction [25])~~ and as building blocks for sensing applications (for example ~~as hotspots in Surface-enhanced Raman Spectroscopy [26],~~ as catalytic agents in electrochemical sensors ~~based on the hydrogen peroxide reduction~~ [26,27] ~~or in the reduction of As(III) [28]~~ and as actuators or hotspots in optical sensors ~~*in vitro*~~ [28–31] ~~and *in vivo* [31]~~). The high interest of these systems in catalysis is due to their improved catalytic performances with respect to the single Au and Fe_3O_4 counterparts, a behavior that was ascribed to the presence of synergistic effects occurring at the interphase between the metallic and the metal oxide counterparts, related to electron transfer phenomena across the interface [32]. Further interest arises from the possibility of magnetic separation from the reaction mixture and from the higher stability of the metallic component against temperature, aggregation and leaching [6].

Within this framework, a significant improvement for the applicability of Au-Fe_3O_4 HNCs is represented by the possibility to finely tune their plasmonic and magnetic properties, and thus to design HNCs with well-defined physico-chemical characteristics. This aspect is particularly relevant concerning the magnetic counterpart, since the use of systems with proper magnetic characteristics (hard or soft magnetic behavior) can strongly improve the specific application. Besides the influence of mean shape and size, it is well known from the literature that the magnetic properties of magnetite NCs can be efficiently tuned also by the partial or total substitution of Fe(II) with other divalent cations, leading to the formation of mixed spinel ferrites [33,34]. For cobalt ferrite $CoFe_2O_4$, the substitution of Fe(II) with Co(II) leads to a strong increase of the magnetic anisotropy with respect to magnetite, both in the bulk and at the nanoscale [35–38]. On the other hand, the total substitution of Fe(II) with Mn(II) (leading to manganese ferrite, $MnFe_2O_4$) causes the increase of the magnetic permeability [37]. Nevertheless, to our knowledge, such high flexibility has been explored so far only for non-epitaxial heterostructures, where the spinel ferrite domains are combined with plasmonic units through simple electrostatic interactions or the mediation of a third material or a functional molecule [39–41]. On the other side, an epitaxial relation grants for a stronger interaction between the two components, largely expanding the potential of the materials. Unfortunately, the literature about magnetic-plasmonic epitaxial HNCs is exclusively focused on Au-Fe_3O_4, except for the work by Guo *et al*. [42], who report the formation of Au-$CoFe_2O_4$ HNCs from laser ablation, a technique less accessible and with a lower degree of control with respect to the standard colloidal syntheses. A similar example of magnetic-plasmonic epitaxial HNCs prepared by a colloidal strategy is based on silver (Ag-$CoFe_2O_4$), [43] which, however, presents different chemical stability and optical properties than Au. However, the synthetic procedure adopted in this case is unsuitable to prepare the Au analogue due to the different reactivity of the metal precursor.

The lack of reports on Au-MFe_2O_4 HNCs (M=Co, Mn, etc…) can be ascribed to the fact that the main synthetic strategy reported in the literature for the preparation of Au-Fe_3O_4 HNCs is based on the use of the iron precursor $Fe(CO)_5$. Indeed, Jiang *et al*. demonstrated that the use of such precursor involves the heteronucleation of metallic iron onto the surface of gold preformed nanoparticles and the successive oxidation to Fe_3O_4 [44]. In these conditions, the formation of mixed spinel ferrite phase is not trivial, and the occurrence of different secondary inorganic phases is highly probable.

With the aim to fill this gap, in this work we present the synthesis of Au-$CoFe_2O_4$ and Au-$MnFe_2O_4$ HNCs by thermal decomposition of the respective acetylacetonate salts in the presence of preformed oleylamine-capped Au NCs. Metal acetylacetonates are commonly used for the synthesis of mixed spinel ferrites nanoparticles [45] and thus they are expected to be better suited for the preparation of Au-MFe_2O_4 HNCs.

The structural, magnetic, optical and magneto-optical characterization indicates the successful epitaxial growth of the ferrite domains onto the gold surface and the effective incorporation of Co(II) and Mn(II) into the lattice, with a consequent variation in the magnetic and magneto-optical properties of the final Au-MFe_2O_4 HNCs.

2. Experimental

2.1 Materials. All samples were prepared under argon atmosphere using commercially available reagents. Cobalt(II) acetylacetonate ($Co(acac)_2{\cdot}2\ H_2O$) (≥99%), manganese(II) acetylacetonate ($Mn(acac)_2$) (≥99.9%), oleylamine (≥98%), oleic acid (90%), 1,2-dodecanediol (90%), benzyl ether (Bz_2O) (98%), 1-octadecene (ODE) (90%), hexane (≥99%), toluene (≥99.7%) and ethanol (99.9%) were purchased from Aldrich Chemical Co. Gold(III) chloride trihydrate ($HAuCl_4\ 3H_2O$) (99.8%) and iron(III) acetylacetonate ($Fe(acac)_3$) (99%) were from Strem Chemicals Co.

2.2 Synthesis of Au NCs. Gold NCs were prepared by reduction of gold(III) chloride trihydrate ($HAuCl_4{\cdot}3H_2O$) by oleylamine at high temperature, using a modified procedure from Hiramatsu *et al*.[46]. A mixture of $HAuCl_4\ 3H_2O$ (120 mg, 0.03 mmol) and oleylamine (3 mL, 9.12 mmol) in phenyl ether (Ph_2O, 20 mL) was heated to 120 ºC at 4 ºC/min with vigorous stirring and kept at this temperature for 45 min. Once the mixture was cooled to room temperature, the obtained Au NCs were precipitated by addition of EtOH (60 mL) and successive centrifugation (4000 rpm, 10 min). This washing procedure was repeated twice. The obtained product could be readily dispersed in hexane or other nonpolar solvents, giving stable suspensions. Transmission Electron Microscopy (TEM) and extinction spectrum of the obtained Au NCs are reported in **Fig. S1** in the Electronic Supplementary Material.

2.3 Synthesis of Au−Fe_3O_4 HNCs. A mixture of $Fe(acac)_3$ (0.177 g, 0.5 mmol), Au NCs (0.011 g in ~5 mL of hexane), oleylamine (0.53 g, 2 mmol), oleic acid (0.565 g, 2 mmol), 1,2-dodecanediol (0.508 g, 2.5 mmol) in 50 mL of solvent (1-octadecene or benzyl ether) was heated up to 205 °C at 5 °C/min under Ar flow and kept at this temperature for 2 h. Then, the reaction was heated up to reflux (315 °C for ODE, 290°C for Bz_2O) at 6 °C/min and kept at this temperature for 2 h before being

let to cool down to room temperature and then exposing it to air. The HNCs suspensions were purified by centrifuging the reaction mixture twice with a mixture of 2-propanol and methanol and re-dispersing it in hexane.

2.4 Synthesis of Au−$CoFe_2O_4$ HNCs. A mixture of $Fe(acac)_3$ (0.117 g, 0.33 mmol), $Co(acac)_2$ (0.05 g, 0.17 mmol), Au NCs (0.011 g in ~5 mL of hexane), oleylamine (0.53 g, 2 mmol), oleic acid (0.565 g, 2 mmol), 1,2-dodecanediol (0.508 g, 2.5 mmol) in 50 mL of solvent (1-octadecene or benzyl ether) was heated up to 205 °C at 5 °C/min under Ar flow and kept at this temperature for 2 h. Then, the reaction was heated up to reflux (315 °C for ODE, 290°C for Bz_2O) at 6 °C/min and kept at this temperature for 2 h before removing it from the heating source, allowing to cool down to room temperature and exposing it to air. The HNCs suspensions were purified by centrifuging the reaction moisture twice with a mixture of 2-propanol and methanol and redispersing it in hexane.

2.5 Synthesis of Au−$MnFe_2O_4$ HNCs. A mixture of $Fe(acac)_3$ (0.117 g, 0.5 mmol), $Mn(acac)_2$ (0.05 g, 0.17 mmol), Au NCs (0.011 g in ~5 mL of hexane), oleylamine (0.53 g, 2 mmol), oleic acid (0.565 g, 2 mmol), 1,2-dodecanediol (0.508 g, 2.5 mmol) in 50 mL of solvent (1-octadecene or benzyl ether) was heated up to 205 °C at 5 °C/min under Ar flow and kept at this temperature for 2 h. Then, the reaction was heated up to reflux (315 °C for ODE, 290°C for Bz_2O) at 6 °C/min and kept at this temperature for 2 h before removing it from the heating source and allowing it to cool down to room temperature before exposing it to air. The HNCs suspensions were purified by centrifuging the reaction product twice with a mixture of 2-propanol and methanol and redispersing it in hexane.

2.6 Structural and magnetic characterization. The morphology, average size and size distribution of the obtained HNCs were determined by TEM using a CM12 PHILIPS microscope operating at 100 kV. Samples were prepared by drop drying a diluted suspension of NCs in hexane onto 200 mesh carbon-coated copper grids. The mean diameter and the size distribution of each sample were obtained by statistical analysis over 300 particles analyzing the recorded images with the ImageJ software.[47] For non-spherical nanostructures, the diameter of the circle that circumscribes the HNCs was considered, while the size estimation of magnetic domains was performed as schematized in **Fig. S2**.

High-resolution TEM images (HRTEM), scanning transmission images in annular dark field mode (STEM-ADF), and energy dispersive X-Ray spectra (EDXS) were acquired at 200 kV on a JEOL JEM-2200FS (HRTEM point resolution 0.19 nm, STEM spot size 2 nm). Elemental maps from Au-M, Fe-K, Co-K, and Mn-K ionization edges were extracted from STEM-EDXS.

Powder XRD measurements were carried out using a Bruker D8 Advance diffractometer equipped with a Cu Kα radiation and operating in θ–θ Bragg Brentano geometry at 40 kV and 40 mA. Lattice parameters, a, and the mean crystallite diameters, d_{XRD}, were evaluated with TOPAS software (Bruker) using the method of Fundamental Parameter Approach, considering a cubic space group $Fd\bar{3}m$ and $Fm\bar{3}m$ for the ferrite and gold phase, respectively.

ICP-AES measurements were performed in triplicate by a Varian 720-ES Inductively Coupled Plasma Atomic Emission Spectrometer, on samples (~1 mg) digested in concentrated *aqua regia* (HCl suprapure and HNO_3 sub-boiled in 3:1 ratio) and in the presence of H_2O_2, diluted with ultrapure water (≥18 MΩ/cm) and analyzed using Ge as internal standard. Calibration standards were prepared by gravimetric serial dilution from mono-standard at 1000 mg/L. The wavelengths used for Co, Fe, Mn and Ge were 238.204, 238.892, 257.610 and 209.426 nm, respectively.

Magnetic measurements were performed using a Quantum Design MPMS SQUID, operating in the 1.8−350 K temperature range and with an applied field up to 5 T. The samples were deposited from hexane suspensions onto a Teflon sample holder, the diamagnetic contribution of which was subtracted during data processing. Zero Field Cooled/ Field Cooled (ZFC/FC) curves were obtained by measuring the temperature dependence of the magnetization applying a probe magnetic field (5 mT), after cooling the sample in the absence (ZFC) or in the presence (FC) of the field.

2.6 Optical and magneto-optical characterization. Optical absorption spectra were recorded on a Jasco V-670 (Jasco Corporation) commercial spectrophotometer in the 300 - 2000 nm range using 5 mL quartz cuvettes.

Magnetic Circular Dichroism (MCD) spectra were recorded in the 300-2000 nm range using an in-house built setup [48] equipped with a 300 W Xe arc lamp coupled to a Oriel 1/4 m Cornerstone 260 monochromator, and a liquid-cooled electromagnet. The setup covers a wavelength range from 300 to 2200 nm and reaches static fields up to 1.4 T at room temperature. Light propagation was set parallel to the static magnetic field. Circular polarization was obtained using a photo-elastic modulator (Hinds Instruments PEM-100) able to switch at a rate of 47 kHz between right- and left-circular light polarization and dichroism was recorded by lock-in detection at the modulation frequency. The differential absorption signal (ΔA) between the two opposite polarizations is retrieved via phase sensitive detection with a lock-in amplifier referenced at the polarization modulation frequency. Offsets and spurious dichroism from the setup were corrected by subtraction of two MCD spectra recorded at the same magnetic field but with opposite sign. The magnitude of dichroism signal (ΔA) was calibrated through a standard technique using a $Fe(CN)_6^{3+}$ solution as a reference. Samples were prepared by mixing 50 µl of each HNCs toluene suspension (~ 1 mg/ml of Au and ~2 mg/ml of Fe+M, where M=Mn, Co) with 100 µl of a poly-methyl-metacrylate (PMMA) solution in toluene (10 % w/w) and casting 50 µl of the mixture on a glass slide and allowing the solvent to evaporate, obtaining thin optically addressable films.

3. Results and discussion

3.1 Synthesis of HNCs. Au-MFe_2O_4 HNCs (M = Fe, Co, Mn) were prepared following the seeded-growth approach described in a previous work for Au-Fe_3O_4 [49], *i.e.* through thermal decomposition of metal acetylacetonates in the presence of oleylamine-capped 10 nm Au NCs. In order to investigate the effect of the reaction solvent on the morphology of the HNCs, the synthesis was repeated in the same conditions but using two solvents with lower and higher polarity, respectively: 1-octadecene (ODE) and benzyl ether (Bz_2O). TEM images (**Fig. 1**) show the formation of monodisperse HNCs when iron (III) acetylacetonate ($Fe(acac)_3$) alone was used as single metal precursor. Consistently with the literature [50,51] and previous observations [49], the morphology of HNCs can be tuned from dimer (Fe-ODE) to flower-like (Fe-Bz_2O) just by increasing the solvent polarity. The size of the iron oxide domains grown onto Au NCs, evaluated as reported in **Fig. S2**, is approximatively constant in both samples

(Table 1~~Table 1~~). Repeating the synthesis using a stochiometric mixture (2:1) of $Fe(acac)_3$ and $Co(acac)_2$ in Bz_2O leads to monodisperse HNCs (Co- Bz_2O) with flower-like morphology and similar mean size as Fe-Bz_2O. However, when the synthesis was carried out in ODE (Co-ODE), flower-like particles were again observed instead of dimers. The occurrence of flower-like morphology was also observed when $Mn(acac)_2$ was used in the reaction mixture with both solvents investigated (**Fig.1**), although with ODE (Mn-ODE) a sizeable secondary population of isolated ferrite nanoparticles occurs. The mean size of ferrite domains in Mn-Bz_2O (~9 nm) was found to be slightly lower than that of Fe-Bz_2O and Co-Bz_2O (~11 nm, Table 1~~Table 1~~).

The M:Fe metal ratios were determined by ICP-AES (**Table S1**). In the case of Co-Bz_2O, the Co:Fe ratio (0.45) was found to be in excellent agreement with that of stochiometric cobalt ferrite $CoFe_2O_4$ (0.5), as a first indication that Co(II) was successfully incorporated into the spinel lattice. However, a value slightly higher than the stoichiometric one was observed for Co-ODE (0.75), suggesting the presence of a secondary cobalt-rich phase, such as CoO or metallic Co. Concerning Au-$MnFe_2O_4$ samples, Mn:Fe lower than the stoichiometric value (~0.21 and ~0.14 for Mn-ODE and Mn Bz_2O, respectively) were observed for both Au-$MnFe_2O_4$ HNCs. A significant reduction of the Mn:Fe values with respect to the ratio of precursors has already been reported by Orbaek *et al.* [52], who attributed this behavior to the higher thermal decomposition temperature of $Mn(acac)_2$ (248°C) with respect to $Fe(acac)_3$ (184°C), resulting in a preferential incorporation of iron ions with respect to manganese ones and thus to a non-stoichiometric manganese ferrite. This hypothesis is consistent with the observation of a higher Mn:Fe ratio for Mn-ODE, for which the reaction temperature was higher (315°C) with respect to Mn-Bz_2O (290°C). Assuming that all the Mn is incorporated in the spinel lattice, the observed Mn:Fe values correspond to the formula $Mn_{0.52}Fe_{2.48}O_4$ and $Mn_{0.38}Fe_{2.62}O_4$ for Mn-ODE and Mn Bz_2O, respectively. From ICP-AES the relative percentage of the magnetic oxide phase and the gold domain was also evaluated. By comparing the samples from the Bz_2O series, we note that Fe-Bz_2O shows a lower Fe:Au ratio (~0.8) with respect to Co-Bz_2O ((Fe+Co):Au ~2.1) and Mn-Bz_2O, ((Fe+Mn):Au ~1.7). These data suggest that in the case of Co-Bz_2O and Mn-Bz_2O a higher number of ferrite domains grow onto the Au surface, and this hypothesis is consistent with TEM images (**Fig. 1**).

Overall, these results suggest that the change of the divalent cation in the metal precursor has a significant effect on the process of formation of HNCs, promoting multiple heterogeneous nucleation onto Au NCs and reducing the influence of the polarity of the reaction solvent on the final morphology when Fe is replaced by Co or Mn. A possible explanation of such behavior can be related to the fact that the different metal-surfactant complexes, formed during the reaction and which decomposition leads to the formation of the spinel ferrite phase, have a different thermal stability and this strongly influences the process of nucleation, *i.e.* number and size of the nuclei formed in the reaction [53].

In order to better highlight the effect of the chemical composition of the spinel ferrite phase on the magnetic and optical properties of Au-MFe_2O_4 HNCs, in the next we will focus only on the series of flower-like samples obtained from Bz_2O (Fe-Bz_2O, Co-Bz_2O, Mn-Bz_2O), which are characterized by a homogeneous morphology and similar mean size. For the sake of completeness, in the Supporting Information we also report the UV-VIS spectra (**Fig. S3**) and the Powder X-ray diffraction (XRD) patterns (**Fig. S4, Table S2**) of the series obtained from ODE (Fe-ODE, Co-ODE, Mn-ODE).

3.2 Structural characterization of HNCs. The XRD patterns of Fe-Bz_2O, Co-Bz_2O and Mn-Bz_2O are reported in **Fig. 2**. For all the samples, the diffraction patterns of two cubic crystalline phases are present, matching in peak position and relative intensity the reference patterns of gold and of the isostructural family of spinel ferrites (magnetite, maghemite, cobalt ferrite, manganese ferrite), without evidence of any additional inorganic phase within the sensitivity range of the instrument. The lattice parameters (a) of the gold and the spinel ferrite phases, reported in Table 2~~Table 2~~, were found to be in good agreement with the reference values. In the case of Fe-Bz_2O, a slightly lower value than the reference one for magnetite (8.396 Å) was observed: this is a feature commonly observed for iron oxide nanoparticles and it is attributed to the partial oxidation of Fe(II) to Fe(III). On the other hand, the value of lattice parameter of Mn-Bz_2O was found much lower (8.419 Å) with respect to the reference value for manganese ferrite (8.499 Å), but consistent with a non-stoichiometric manganese ferrite $Mn_xFe_{3-x}O_4$, as already suggested by ICP-AES.

The mean crystalline sizes of Au and spinel ferrite domains, evaluated from XRD patterns, are reported in Table 2~~Table 2~~. As observed previously on Au-Fe_3O_4 HNCs and Au NCs [49], the crystalline size of Au was found to be smaller with respect to the NCs size obtained by TEM, feature which can be related to its polycrystalline multiply-twinned structure. Concerning MFe_2O_4 domains, the direct comparison of mean size values obtained by TEM (d_{TEM}) and XRD (d_{XRD}) is less trivial, mainly due to the irregular shape of these counterparts. However, an excellent agreement was found for Fe-Bz_2O and Co-Bz_2O, suggesting the high crystallinity of the ferrite domains. On the other hand, in the case of Mn-Bz_2O a lower value of d_{XRD} with respect to d_{TEM} suggests a slightly lower crystalline degree.

HRTEM images of the flower-like Au-MFe_2O_4 HNCs (**Fig. 3**) confirmed the high crystallinity of both Au and MFe_2O_4 domains. Epitaxial relationships along the cubic directions were observed in all the samples. In particular (220)Au//(220)Fe_3O_4 or (111)Au//(111)Fe_3O_4 epitaxial relations were observed in agreement with our previous report [49]. In order to investigate the distribution of the different metals within the HNCs, STEM-EDXS elemental maps were recorded and compared to the STEM-ADF reference images (**Fig. 4** and **Fig. S5**). The distribution of Co and Mn was found to be homogeneous and co-localized with Fe, confirming thus the successful incorporation of these metals within the spinel lattice of magnetite. The obtained M:Fe ratio (0.38 for M=Co and 0.11 for M=Mn) were found to be in good agreement with values obtained from ICP-AES.

The whole structural characterization clearly confirms the formation of a highly crystalline cubic spinel ferrite phase, epitaxially grown onto the top of the preformed Au NCs. In the case of Mn-Bz_2O, the formation of a non-stoichiometric manganese ferrite is confirmed both by STEM-EDXS elemental maps and by the observation of a lower lattice parameter. As discussed in the previous paragraph, the formation of a non-stoichiometric manganese ferrite can be ascribed in first instance to a different decomposition temperature of $Mn(acac)_2$ and $Fe(acac)_3$. Moreover, the large lattice parameter of manganese ferrite can represent an additional driving force towards the lower

incorporation of Mn ions in the ferrite lattice. Indeed, the process of heterogeneous nucleation between two materials will be more or less favored depending of the lattice mismatch between the two crystalline phases. In the case of Au-$MnFe_2O_4$ HNCs, the lattice mismatch is higher (~4%) than for Au-Fe_3O_4 HNCs (~3%), therefore the heterogenous nucleation of stoichiometric manganese ferrite is expected to be less favored with respect to that of magnetite. It is thus reasonable that the minimization of the mismatch is an additional cause for the low inclusion of Mn ions in the spinel lattice. Such hypothesis is consistent with the observation that when the reaction is carried out in ODE an increase of Mn:Fe ratio and therefore of the lattice parameter, occurs. In these conditions, the process of heterogeneous nucleation could be then less favored with respect to the homogeneous one, leading to the formation of a secondary population of isolated $Mn_xFe_{3-x}O_4$.

Overall, these results demonstrate that it is possible to modify the spinel ferrite composition of Au-MFe_2O_4 HNCs with neither affecting their shape, average size and crystalline quality nor observing the formation of secondary undesired phases.

Nano Research

ISSN 1998-0124 CN 11-5974/O4
https://doi.org/(automatically inserted by the publisher)

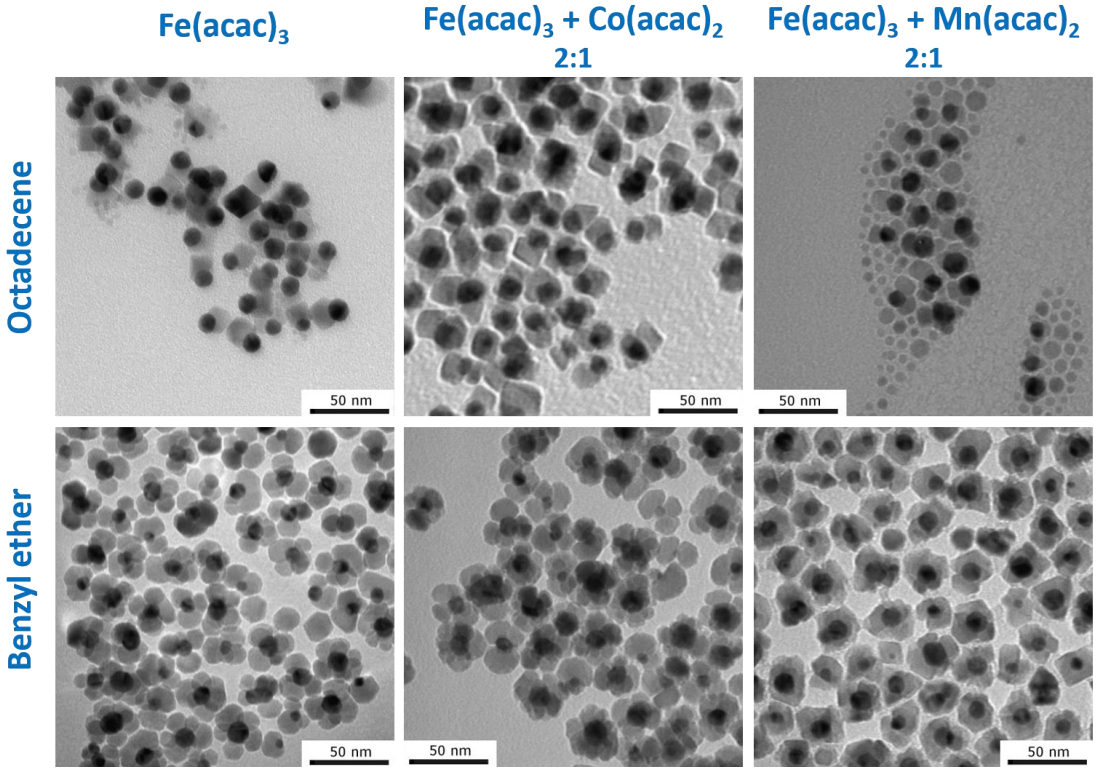

Figure 11 Representative TEM images of Au-MFe_2O_4 HNCs samples prepared by acetylacetonate precursors

Table 11 Mean size, d_{TEM} *(nm)*, of Au-MFe_2O_4 HNCs and of each component (MFe_2O_4 and Au domains), obtained from TEM analysis, according to the scheme of **Fig. S2**.

Sample	Fe-ODE	Fe-Bz_2O	Co-ODE	Co-Bz_2O	Mn-ODE	Mn-Bz_2O
HNCs	23 ± 4	32 ± 5	27 ± 6	31 ± 5	24 ± 4	29 ± 4
MFe_2O_4	11 ± 3	11 ± 2	10 ± 3	11 ± 2	7 ± 2	9 ± 2
Au	13 ± 1	11 ± 2	13 ± 3	10 ± 2	12 ± 2	11 ± 3

Table 22 Structural and optical properties of Au-MFe_2O_4 HNCs.

	HNCs	MFe_2O_4			Au			HNCs
Sample	d_{TEM} (nm)	d_{TEM} (nm)	d_{XRD} (nm)	a (Å)	d_{TEM} (nm)	d_{XRD} (nm)	a (Å)	λ_{max} (nm)
Fe-Bz_2O	32 ± 5	11 ± 2	10.4 ± 0.3	8.376(3)	11 ± 2	5.98 ± 0.09	4.077(1)	594
Co-Bz_2O	31 ± 5	11 ± 2	10.8 ± 0.2	8.402(2)	10 ± 2	5.11 ± 0.02	4.081(1)	574
Mn-Bz_2O	29 ± 4	9 ± 2	6.9 ± 0.2	8.419(4)	11 ± 3	5.27 ± 0.08	4.082(2)	602

d_{TEM}: HNCs average diameter and standard deviation obtained from TEM analysis; a and d_{XRD}: lattice parameter and crystallite mean size obtained from XRD data analysis (errors are reported in brackets), respectively; λ_{max}: wavelength of the plasmonic resonance.

3.3 Optical, magnetic and magneto-optical characterization of HNCs. The optical properties of flower-like Au-$MnFe_2O_4$ HNCs were investigated by recording extinction spectra in the UV-visible-NIR range on toluene suspensions (**Fig. 5**). All samples show a well-defined Localized Surface Plasmon Resonance (LSPR) peak, which is red-shifted and slightly damped with respect to the starting Au NCs used as seeds. Such behavior is commonly observed in dimer and flower-like Au-Fe_3O_4 heterostructured nanocrystals [10,49,51,54–56] and it can be rationalized considering the presence of an oxide layer in direct contact at the Au NCs surface [57,58].

Interestingly, the plasmonic resonance was found to depend on the chemical composition of the spinel ferrite, with a larger red-shift for Fe-Bz_2O (594 nm) and Mn-Bz_2O (604 nm) with respect to Co-Bz_2O (574 nm). This behavior is probably related to small differences in the morphology of the samples, rather than to the specific dielectric functions of the three ferrites.

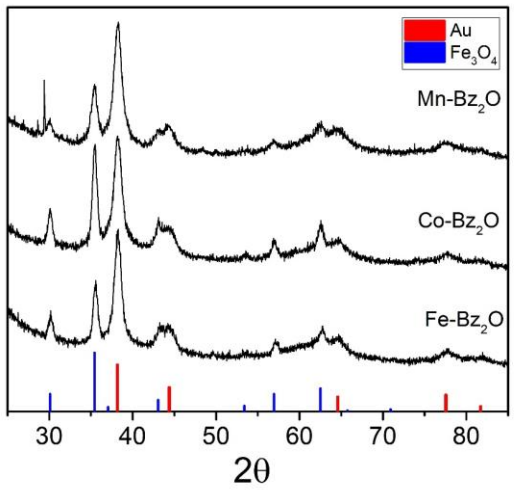

Figure 22~~2~~ X-ray powder diffraction patterns of Fe-Bz_2O, Co-Bz_2O and Mn-Bz_2O, together with the reference patterns of magnetite (PDF 19-0629, blue) and gold (PDF 04-0784, red).

The magnetization of the flower-like Au-MFe_2O_4 HNCs series prepared in Bz_2O (Fe-Bz_2O, Co-Bz_2O, Mn-Bz_2O) was investigated as a function of the magnetic field both at low (5 K) and room (300 K) temperature (**Fig. 6a-b**) by SQUID magnetometry. For all the samples, low magnetic saturation values, M_S, per mass of sample were observed, due to the high percentage of diamagnetic gold. However when normalized by the effective amount of magnetic metals obtained from ICP-AES (Table 33~~Table 3~~), M_S rescale to values close to the respective literature reference values for nanosized spinel ferrites in the case of Fe-Bz_2O and Co-Bz_2O [36,59], taking into account the error related to the determination of the amount of magnetic metals in the sample, estimated around 10% (see caption Table 3). On the other hand, for Mn-Bz_2O a slightly lower value of M_S was observed with respect to the literature [60,61]. Such behavior can be ascribed to a reduced crystallinity of the ferrite domains, as evidenced by XRD measurements, and to a magnetic disorder induced by Mn ions substitution in the spinel structure. However, this last hypothesis should be confirmed by further investigation that is beyond the purpose of this work. At room temperature, Fe-Bz_2O and Mn-Bz_2O show superparamagnetic behavior, while Co-Bz_2O exhibits a hysteretic behavior with coercive field of 44 mT. On the other hand, at low temperature all the samples show an open hysteresis loop, with a much larger coercive field observed for sample Co-Bz_2O (1.21 T) with respect to Fe-Bz_2O (37 mT) and Mn-Bz_2O (46 mT). Such strong increase of the coercive field is related to the significant increase of the magnetic anisotropy of the material, a feature that clearly indicates that Co(II) ions were successfully introduced into the spinel lattice. Focusing on the hysteresis curves at room temperature, it is possible to note that Mn-Bz_2O shows a different approach to saturation with respect to Fe-Bz_2O and Co-Bz_2O, characterized by a higher slope of the magnetization at high field. This behavior suggests a higher magnetic disorder in Mn-Bz_2O, which is consistent with the lower value of saturation magnetization observed with respect to the literature ones for $MnFe_2O_4$ NCs and with the smaller mean size of the MFe_2O_4 domains evaluated from XRD with respect to that of TEM (Table 22~~Table 2~~).

The temperature dependence of the magnetization was investigated after a procedure of zero field cooling (ZFC) and field cooling with a magnetic field of 5 mT (FC) (**Fig. 6c**). All samples show the typical thermal irreversibility of nanosized magnetic materials and the plateau of the FC curve at low temperature indicates an ensemble of strongly interacting magnetic nanoparticles. The blocking temperature, T_B, commonly identified as the temperature where the ZFC curve reaches its maximum, is not well defined for Fe-Bz_2O and Co-Bz_2O, because the ZFC curves do not reach a maximum in the measuring range. However, the curve shape clearly suggests T_B very close to room temperature for Fe-Bz_2O and much higher for Co-Bz_2O, coherently with the increase of magnetic anisotropy. On the other hand, the lower T_B (280 K) observed for Mn-Bz_2O is consistent with the smaller mean size of the ferrite domains and with the higher crystalline and magnetic disorder.

Importantly, the data here presented confirm that it is possible to significantly tune the magnetic properties of Au-MFe_2O_4 HNCs by a simple chemical modification of the magnetic component while preserving a well-defined plasmonic response.

In order to have a better insight on the electronic structure of the spinel phases and on the possible interplay between magnetic and plasmonic components, the flower-like Au-MFe_2O_4 HNCs were investigated through Magnetic Circular Dichroism (MCD). This technique is very sensitive to small changes in the electronic structure of magnetic materials, and is a powerful tool to detect changes in the chemical composition of spinel ferrites [62,63]. MCD spectra of Fe-Bz_2O, Co-Bz_2O and Mn-Bz_2O dispersed in PMMA matrix, reported in **Fig. 7**, show complex profiles involving several transitions and significant differences can be observed among the samples. The interpretation of the MCD spectra of iron oxide and other spinel ferrites is not straightforward, due to their complex electronic structure. The possible electronic transitions for these systems can be divided in two main classes: i) crystal field transitions (CF) between the 3d states of single metal ions, split in energy due to the ligand field of the surroundings oxygens; ii) charge transfer transitions (CT), which involve different metal ions and which can then be further divided in Intervalence CT (IVCT), in which one electron is transferred to a neighbor cation, and Intersublattice CT (ISCT), occurring between cations in different crystallographic sites. Several interpretations in the assignments of the magneto-optical (MO) transitions have been proposed in the literature: for the purpose of this work, we adopt that of Fontijn *et al.* [64], which to date represents the most complete and systematic overview of the MO properties of spinel ferrites. In the followings, square and round brackets indicate ions in octahedral and tetrahedral coordination, respectively.

Nano Research

ISSN 1998-0124 CN 11-5974/O4
https://doi.org/(automatically inserted by the publisher)

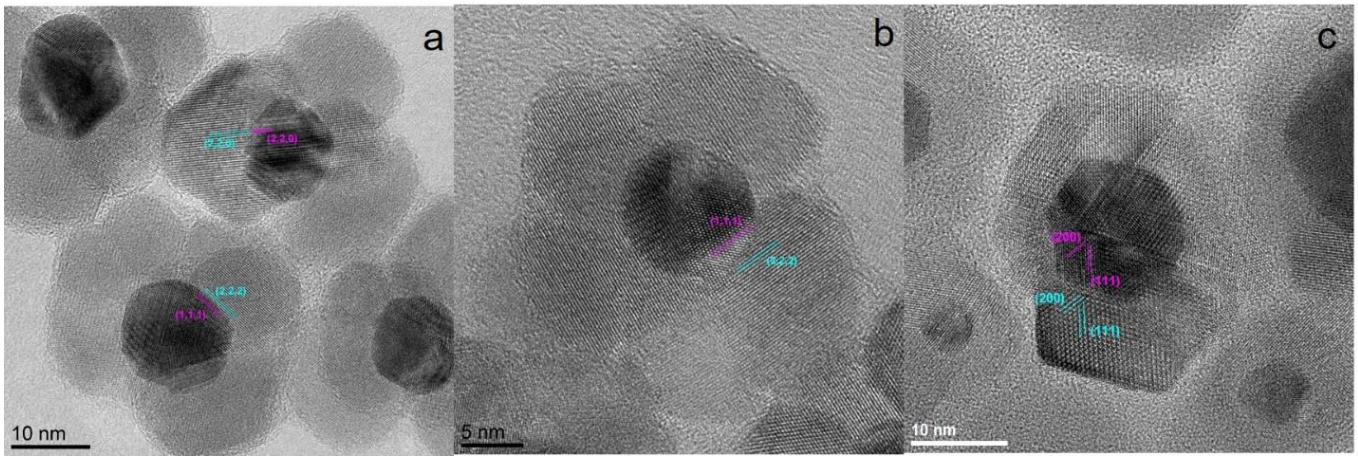

Figure ~~333~~ High-resolution images of samples a) Fe-Bz_2O, b) Co-Bz_2O, c) Mn-Bz_2O.

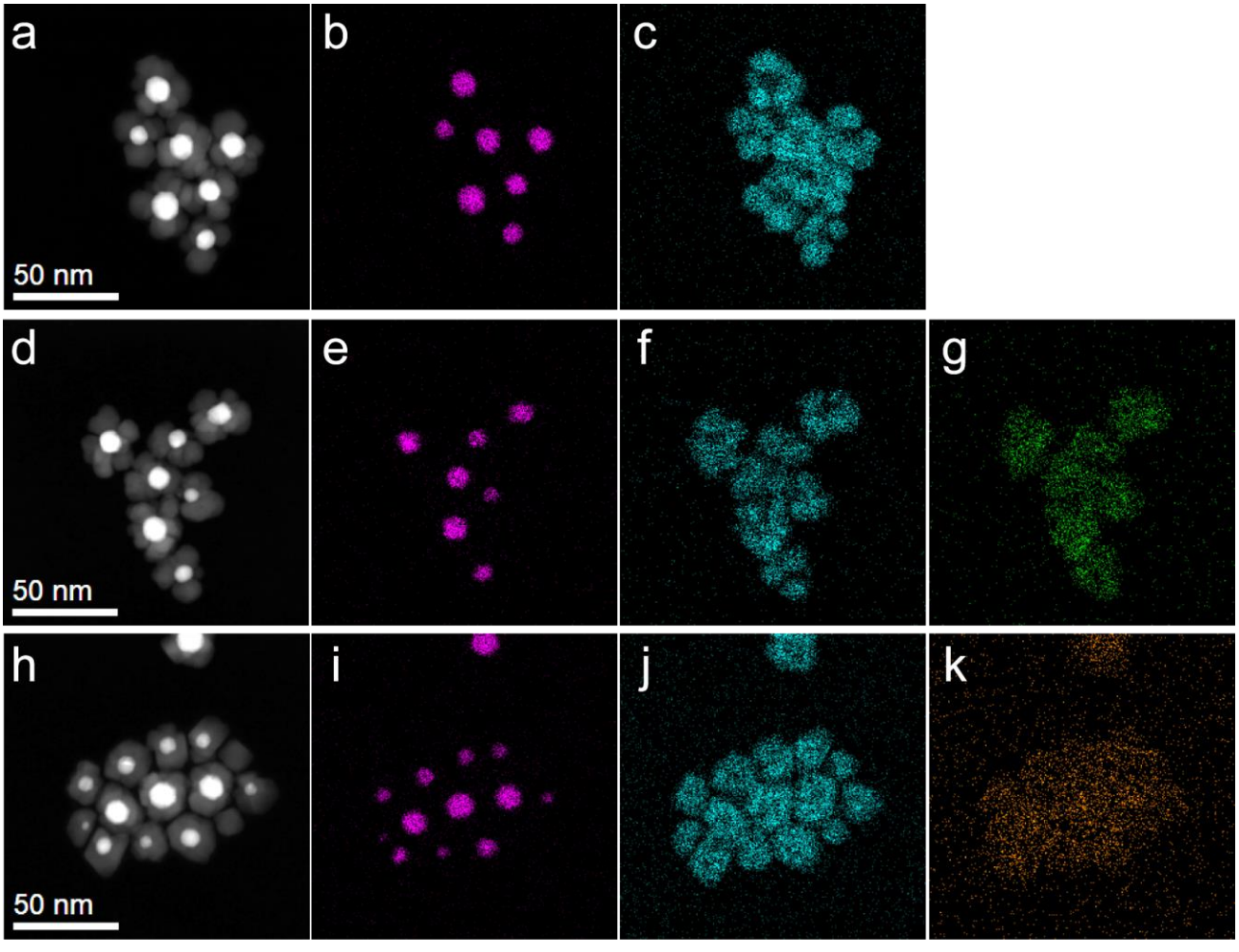

Figure ~~444~~ STEM-EDXS elemental mapping of Fe-Bz_2O (a-c), Co-Bz_2O (d-g) and Mn- Bz_2O (h-k). STEM-ADF reference image (a, d, h); Au mapping images (b, e, i); Fe mapping images (c, f, j); Co mapping image (g); Mn mapping image (k). For each sample, chemical maps were collected using the same experimental settings (spot size and dwell time).

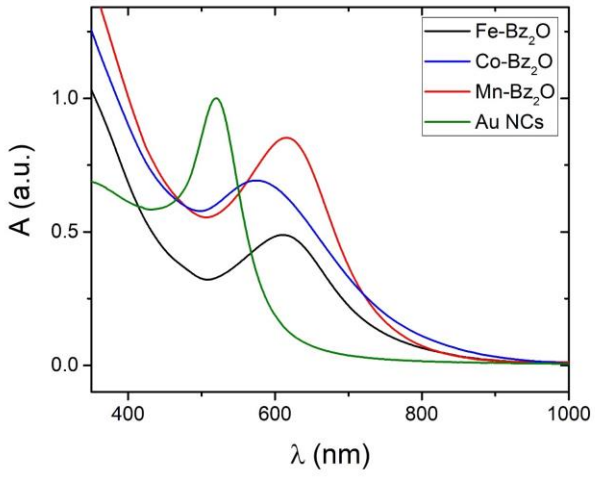

Figure 555 Extinction spectra of Fe-Bz_2O (black), Co-Bz_2O (blue) and Mn-Bz_2O (red), together with the Au NCs used as seeds (green).

The MCD spectra of Fe-Bz_2O and Mn-Bz_2O show the presence of a broad peak in the near infrared region (nIR), centered around ~1560 nm and ~1764 nm, respectively. This transition can be attributed to an IVCT involving both Fe^{3+} and Fe^{2+}, i.e. a transition $[Fe^{3+}]_{t2g} \rightarrow [Fe^{2+}]_{t2g}$, and its presence in Mn-Bz_2O is consistent with a non-stoichiometric manganese ferrite, as evidenced by structural and chemical characterization. A similar broad peak can be observed also in Co-Bz_2O, however in this case it is superimposed to a strong transition with derivative shape, centered at ~1557 nm and ascribed to the CF transition $^4A_2 \rightarrow {}^2T_1(F)$, characteristic of Co^{2+} in tetrahedral coordination. Another significant fingerprint of Co^{2+} in Co-Bz_2O spectrum is the intense peak at ~730 nm, which can be ascribed to the CF transition $^4A_2 \rightarrow {}^2T_1(P)$, again related to Co^{2+} in tetrahedral coordination. A shoulder of the latter peak, localized around 594 nm, can be identified as the IVCT between a divalent ion and Fe^{3+} in octahedral sites, i.e. $[M^{2+}] \rightarrow [Fe^{2+}]_{t2g}$. We did not expect to observe an analogue transition in Mn-Bz_2O sample, since from the literature manganese has a strong preference for tetrahedral sites of the cubic spinel lattice [33].

In the 300-500 nm range, an intense peak is observed for Fe-Bz_2O and Mn-Bz_2O (centered around 430 and 446 nm, respectively), which can be ascribed to the IVCT transition $[Fe^{2+}]_{t2g} \rightarrow (Fe^{2+})_e$: indeed, the transition is observed in Mn-Bz_2O, which has a non-stoichiometric composition and thus contains a large amount of Fe^{2+}, and it is not expected for Co-Bz_2O. Finally, in all samples a peak around 375 nm can be observed (even if highly damped in the case of Mn-Bz_2O), which can be identified as the ISCT transition $[Fe^{3+}]_{eg} \rightarrow (Fe^{2+})_{t2}$.

In a magnetic-plasmonic system, both the magneto-optical fingerprints of the magnetic and the plasmonic moieties are expected. The latter is in general much weaker than the former. It is known that non-magnetic systems supporting localized plasmon resonance give a magneto-optical response, arising from the mode splitting induced by the applied magnetic field [65–67]. Starting from the optical line shape of the LSPR, it is possible to accurately calculate the magneto-optical signature of the plasmonic moiety, assuming that no interaction with the magnetic component is taking place. In order to check this point, we fitted the optical absorption spectra of the polymer-cast HNC samples (**Fig. S6**; see ESM for details and fitting results). Each spectrum was fitted as the sum of a Lorentzian peak arising from LSPR, and a Gaussian peak

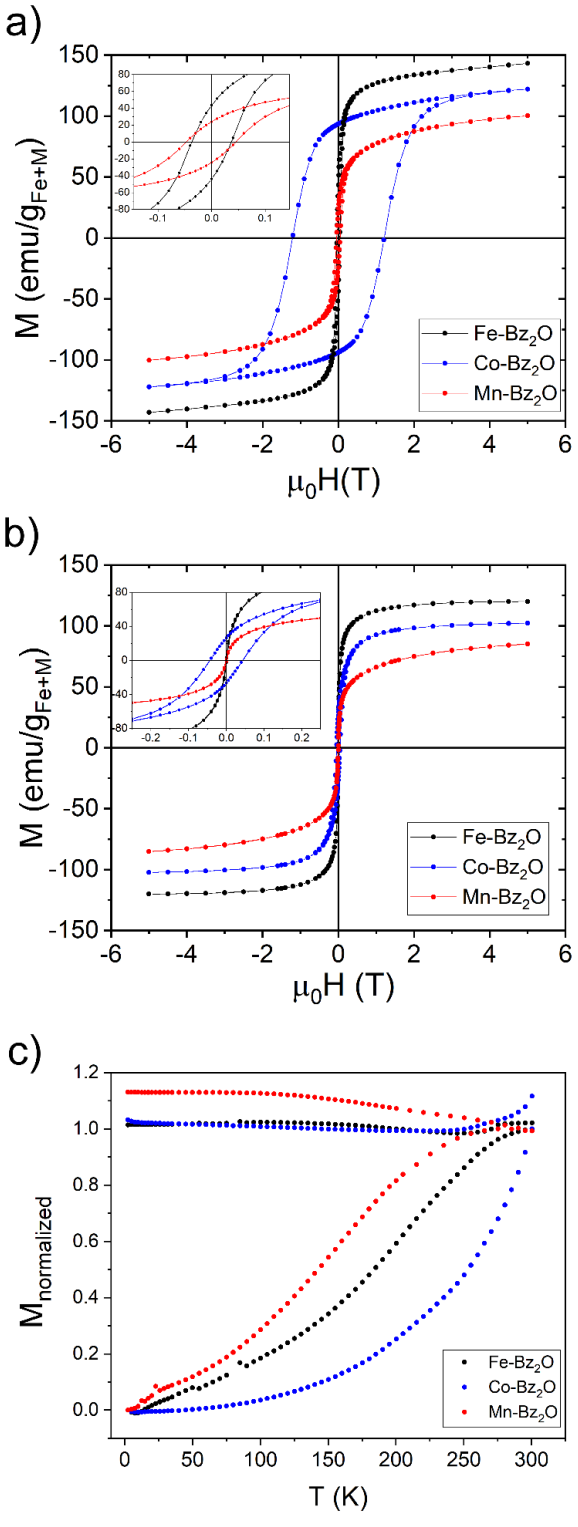

Figure 666 a, b) Magnetization curves of Au-MFe_2O_4 HNCs recorded at 5 K (a) and 300 K (b). In the inset, the magnification of the low field region is shown. c) Temperature dependence of the magnetization after a procedure of Zero Field Cool (ZFC) and Field Cool (FC). Each curve is normalized to the corresponding maximum value of the ZFC curve.

approximating high energy interband transitions (**Fig. S7**). The plasmonic contribution of LSPR to the MCD spectrum was then simulated by calculating the difference of two Lorentzian line shapes, the parameters of which were taken from fitting of the

optical peak, and imposing a shift of ± half the cyclotron energy to the LSPR energy $\hbar\omega_{\pm} = \hbar\omega_0 \pm \hbar eB/2m_e$. The calculated plasmonic contributions to the MCD spectra are reported along with the experimental spectra of each sample in **Fig. S8**. It is clear that in all samples the plasmonic contribution is negligible compared to that of the oxide, and that the MCD spectrum of each HNC system is dominated by the magnetic component. In case of a magnetoplasmonic coupling between the two moieties, the expected line shape would have been the derivative-like signal of the plasmon, but with an increased intensity [68]. While this finding is a downside from the point of view of applicability of these systems as magnetoplasmonic vectors, this type of analysis demonstrates a high degree of predictivity in terms of magnetoplasmonic effects.

4. Conclusions

In conclusion, we have shown that the magnetic properties of gold/spinel ferrite HNCs can be efficiently tuned by partial substitution of the divalent metal ions without affecting the optical properties. Au-MFe_2O_4 HNCs (M = Fe, Co, Mn) were in fact successfully synthesized by a seeded-growth approach based on thermal decomposition of metal acetylacetonates in the presence of preformed Au-NCs capped with oleylamine. Interestingly, the HNCs' morphology changes from dimer to flower-like depending on the solvent polarity and divalent metal cation used. A complete structural characterization by XRD and HR-TEM demonstrates the epitaxial growth of MFe_2O_4 onto the gold phase and the effective incorporation of cobalt and manganese ions within the spinel lattice. Consequently, the magnetic properties reflect the change of composition: a strong enhancement of the magnetic anisotropy is observed for Au-$CoFe_2O_4$ HNCs while in the case of Au-$MnFe_2O_4$ HNCs the expected increase of magnetic moment is masked by the structural and magnetic disorder which characterizes Mn substitution. Finally, all samples were found to retain a plasmonic resonance after the coupling with the spinel ferrite phases, showing well defined plasmonic peaks slightly damped and red-shifted with respect to the pristine Au NCs. The overall physical properties of the presented HNCs and the possibility of modifying them according to the requirements of the specific applications make them useful building blocks for assembling a new generation of biomedical devices. Moreover, the growth of the ferrite domains on the gold cores induces a significant shift of the plasmonic response towards the nIR region, a spectral region characterized by a higher transparency of living tissues and thus of high interest for optical imaging and photothermal therapy. Therefore, given its general validity, the proposed approach can be viewed as a promising starting point for the design of magnetic-plasmonic theranostic agents with optimized properties.

Table 333 Magnetic properties of Au-MFe_2O_4 HNCs.

		5 K			300 K		
sample	T_B[a] (K)	$\mu_0 H_C$ (mT)[b]	M_{5T} ($Am^2/kg_{(Fe+M)}$)[c]	M_R[d]	$\mu_0 H_C$ (mT)[b]	M_{5T} ($Am^2/kg_{(Fe+M)}$)[c]	M_R[d]
Fe-Bz_2O	~300	37	143	0.30	-	120	-
Co-Bz_2O	>300	1210	122	0.77	44	102	0.26
Mn-Bz_2O	280	46	100	0.25	-	85	-

[a] Blocking temperature evaluated as the maximum of the ZFC-FC curve [b] $\mu_0 H_C$: coercive field; [c] M_{5T}: experimental magnetization measured at 5 T normalized by the total amount of Fe+M (M=Co, Mn), taken as an estimate of the saturation value, M_S; [d] M_R: reduced remnant magnetization (M_{0T}/M_{5T}). Errors on direct experimental measurement of $\mu_0 H_C$ and M_R can be estimated to be less than 1‰, while the uncertainty on T_B can be considered as the half-interval between the temperature of two subsequent acquisition points (2.5 K). The error on M_{5T} is estimated around 10% and this mainly correlated to the accuracy of the measurement of the total amount of Fe+M (M=Co, Mn) by ICP.

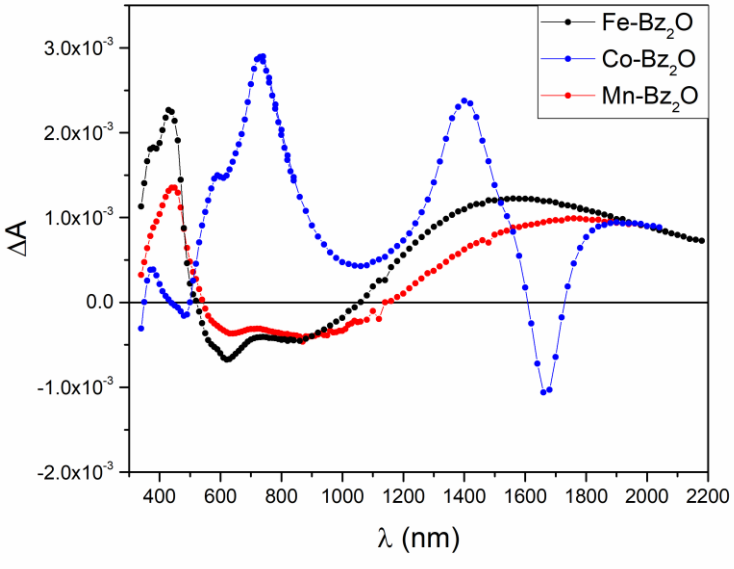

Figure 777 MCD spectra of Au-MFe_2O_4 HNCs.

Nano Research

ISSN 1998-0124 CN 11-5974/O4
https://doi.org/(automatically inserted by the publisher)

Acknowledgements

The financial support of European Union's Horizon2020 Research and Innovation program under Grant agreements No. 737093 (FEMTOTERABYTE, http://www.physics.gu.se/femtoterabyte) and No. 720853 (AMPHIBIAN, http://amphibianproject.eu/), University of Pisa through project PRA_2017_25 and INFN through HADROMAG project is gratefully acknowledged. E.F. thanks the support of the "Galileo Galilei" fellowship from the University of Pisa.

Electronic Supplementary Material: Supplementary material (TEM image and extinction spectra of Au NCs; metal to iron ratios obtained from ICP; UV-VIS spectra, XRD patterns of Au−MFe_2O_4 HNCs (M = Fe, Co, Mn) prepared in 1-octadecene; STEM-HAADF images of Au−MFe_2O_4 HNCs (M = Fe, Co, Mn) prepared in benzyl ether; extinction spectra of Au−MFe_2O_4 HNCs (M = Fe, Co, Mn) in PMMA, details on fitting procedure of the optical extinction spectra of the HNCs, fitting results, calculated MCD contributions of the plasmonic components of the HNCs along with experimental MCD spectra) is available in the online version of this article at http://dx.doi.org/10.1007/s12274-***-****-* (automatically inserted by the publisher).

References

[1] Scarfiello, R.; Nobile, C.; Cozzoli, P.D. Colloidal Magnetic Heterostructured Nanocrystals with Asymmetric Topologies: Seeded-Growth Synthetic Routes and Formation Mechanisms. *Front. Mater.*, **2016**, *3*, 1–29.

[2] Cozzoli, P.D.; Pellegrino, T.; Manna, L. Synthesis, properties and perspectives of hybrid nanocrystal structures. *Chem. Soc. Rev.*, **2006**, *35*, 1195–1208.

[3] Lee, N.; Yoo, D.; Ling, D.; Cho, M.H.; Hyeon, T.; Cheon, J. Iron Oxide Based Nanoparticles for Multimodal Imaging and Magnetoresponsive Therapy. *Chem. Rev.*, **2015**, *115*, 10637–10689.

[4] De La Vega, J.C.; Häfeli, U.O. Utilization of nanoparticles as X-ray contrast agents for diagnostic imaging applications. *Contrast Media Mol. Imaging*, **2015**, *10*, 81–95.

[5] Yang, X.; Yang, M.; Pang, B.; Vara, M.; Xia, Y. Gold Nanomaterials at Work in Biomedicine. *Chem. Rev.*, **2015**, *115*, 10410–10488.

[6] Leung, K.C.-F.; Xuan, S.; Zhu, X.; Wang, D.; Chak, C.-P.; Lee, S.-F.; Ho, W.K.-W.; Chung, B.C.-T. Gold and iron oxide hybrid nanocomposite materials. *Chem. Soc. Rev.*, **2012**, *41*, 1911–1928.

[7] Nguyen, T.; Mammeri, F.; Ammar, S. Iron Oxide and Gold Based Magneto-Plasmonic Nanostructures for Medical Applications: A Review. *Nanomaterials*, **2018**, *8*, 149.

[8] Tian, X.; Zhang, L.; Yang, M.; Bai, L.; Dai, Y.; Yu, Z.; Pan, Y. Functional magnetic hybrid nanomaterials for biomedical diagnosis and treatment. *Wiley Interdiscip. Rev. Nanomedicine Nanobiotechnology*, **2018**, *10*, e1476.

[9] Choi, S.-H.; Na, H. Bin; Park, Y. Il; An, K.; Kwon, S.G.; Jang, Y.; Park, M.; Moon, J.; Son, J.S.; Song, I.C.; Moon, W.K.; Hyeon, T. Simple and Generalized Synthesis of Oxide−Metal Heterostructured Nanoparticles and their Applications in Multimodal Biomedical Probes. *J. Am. Chem. Soc.*, **2008**, *130*, 15573–15580.

[10] Umut, E.; Pineider, F.; Arosio, P.; Sangregorio, C.; Corti, M.; Tabak, F.; Lascialfari, A.; Ghigna, P. Magnetic, optical and relaxometric properties of organically coated gold–magnetite (Au–Fe_3O_4) hybrid nanoparticles for potential use in biomedical applications. *J. Magn. Magn. Mater.*, **2012**, *324*, 2373–2379.

[11] Efremova, M. V.; Naumenko, V.A.; Spasova, M.; Garanina, A.S.; Abakumov, M.A.; Blokhina, A.D.; Melnikov, P.A.; Prelovskaya, A.O.; Heidelmann, M.; Li, Z.A.; Ma, Z.; Shchetinin, I. V.; Golovin, Y.I.; Kireev, I.I.; Savchenko, A.G.; Chekhonin, V.P.; Klyachko, N.L.; Farle, M.; Majouga, A.G.; Wiedwald, U. Magnetite-Gold nanohybrids as ideal all-in-one platforms for theranostics. *Sci. Rep.*, **2018**, *8*, 1–19.

[12] Xu, C.; Xie, J.; Ho, D.; Wang, C.; Kohler, N.; Walsh, E.G.; Morgan, J.R.; Chin, Y.E.; Sun, S. Au–Fe_3O_4 Dumbbell Nanoparticles as Dual-Functional Probes. *Angew. Chemie Int. Ed.*, **2008**, *47*, 173–176.

[13] Kim, D.; Yu, M.K.; Lee, T.S.; Park, J.J.; Jeong, Y.Y.; Jon, S. Amphiphilic polymer-coated hybrid nanoparticles as CT/MRI dual contrast agents. *Nanotechnology*, **2011**, *22*, 155101.

[14] Zhu, J.; Lu, Y.; Li, Y.; Jiang, J.; Cheng, L.; Liu, Z.; Guo, L.; Pan, Y.; Gu, H. Synthesis of Au–Fe_3O_4 heterostructured nanoparticles for in vivo computed tomography and magnetic resonance dual model imaging. *Nanoscale*, **2014**, *6*, 199–202.

[15] Espinosa, A.; Bugnet, M.; Radtke, G.; Neveu, S.; Botton, G.A.; Wilhelm, C.; Abou-Hassan, A. Can magneto-plasmonic nanohybrids efficiently combine photothermia with magnetic hyperthermia? *Nanoscale*, **2015**, *7*, 18872–18877.

[16] Guardia, P.; Nitti, S.; Materia, M.E.; Pugliese, G.; Yaacoub, N.; Greneche, J.M.; Lefevre, C.; Manna, L.; Pellegrino, T. Gold-iron oxide dimers for magnetic hyperthermia: The key role of chloride ions in the synthesis to boost the heating efficiency. *J. Mater. Chem. B*, **2017**, *5*, 4587–4594.

[17] Xu, C.; Wang, B.; Sun, S. Dumbbell-like Au−Fe_3O_4 Nanoparticles for Target-Specific Platin Delivery. *J. Am. Chem. Soc.*, **2009**, *131*, 4216–4217.

[18] Kakwere, H.; Materia, M.E.; Curcio, A.; Prato, M.; Sathya, A.; Nitti, S.; Pellegrino, T. Dually responsive gold-iron oxide heterodimers: Merging stimuli-responsive surface properties with intrinsic inorganic material features. *Nanoscale*, **2018**, *10*, 3930–3944.

[19] Yin, H.; Wang, C.; Zhu, H.; Overbury, S.H.; Sun, S.; Dai, S. Colloidal deposition synthesis of supported gold nanocatalysts based on Au–Fe_3O_4 dumbbell nanoparticles. *Chem. Commun.*, **2008**, 4357.

[20] Najafishirtari, S.; Guardia, P.; Scarpellini, A.; Prato, M.; Marras, S.; Manna, L.; Colombo, M. The effect of Au domain size on the CO oxidation catalytic activity of colloidal Au–FeO_x dumbbell-like heterodimers. *J. Catal.*, **2016**, *338*, 115–123.

[21] Wang, C.; Yin, H.; Dai, S.; Sun, S. A general approach to noble metal-metal oxide dumbbell nanoparticles and their catalytic application for CO oxidation. *Chem. Mater.*, **2010**, *22*, 3277–3282.

[22] Najafishirtari, S.; Guardia, P.; Scarpellini, A.; Prato, M.; Marras, S.; Manna, L.; Colombo, M. The effect of Au domain size on the CO oxidation catalytic activity of colloidal Au–FeOx dumbbell-like heterodimers. *J. Catal.*, **2016**, *338*, 115–123.

[23] Lee, Y.; Garcia, M.A.; Frey Huls, N.A.; Sun, S. Synthetic Tuning of the Catalytic Properties of Au-Fe_3O_4 Nanoparticles. *Angew. Chemie Int. Ed.*, **2010**, *49*, 1271–1274.

[24] Lin, F.H.; Doong, R.A. Bifunctional Au-Fe_3O_4 heterostructures for magnetically recyclable catalysis of nitrophenol reduction. *J. Phys. Chem. C*, **2011**, *115*, 6591–6598.

[25] Strickler, A.L.; Escudero-Escribano, M.; Jaramillo, T.F. Core-Shell Au@Metal-Oxide Nanoparticle Electrocatalysts for Enhanced

Oxygen Evolution. *Nano Lett.*, **2017**, *17*, 6040–6046.

[26] Wei, Q.; Xiang, Z.; He, J.; Wang, G.; Li, H.; Qian, Z.; Yang, M. Dumbbell-like Au-Fe_3O_4 nanoparticles as label for the preparation of electrochemical immunosensors. *Biosens. Bioelectron.*, **2010**, *26*, 627–631.

[27] Li, S.S.; Zhou, W.Y.; Jiang, M.; Guo, Z.; Liu, J.H.; Zhang, L.; Huang, X.J. Surface Fe(II)/Fe(III) Cycle Promoted Ultra-Highly Sensitive Electrochemical Sensing of Arsenic(III) with Dumbbell-Like Au/Fe_3O_4 Nanoparticles. *Anal. Chem.*, **2018**, *90*, 4569–4577.

[28] Shen, J.; Yang, Y.; Zhang, Y.; Yang, H.; Zhou, Z.; Yang, S. Functionalized Au-Fe_3O_4 nanocomposites as a magnetic and colorimetric bimodal sensor for melamine. *Sensors Actuators, B Chem.*, **2016**, *226*, 512–517.

[29] Zhang, Y.; Zhao, Y.; Yang, Y.; Shen, J.; Yang, H.; Zhou, Z.; Yang, S. A bifunctional sensor based on Au-Fe_3O_4 nanoparticle for the detection of Cd^{2+}. *Sensors Actuators B Chem.*, **2015**, *220*, 622–626.

[30] Reguera, J.; Jiménez De Aberasturi, D.; Winckelmans, N.; Langer, J.; Bals, S.; Liz-Marzán, L.M. Synthesis of Janus plasmonic-magnetic, star-sphere nanoparticles, and their application in SERS detection. *Faraday Discuss.*, **2016**, *191*, 47–59.

[31] Xie, J.; Zhang, F.; Aronova, M.; Zhu, L.; Lin, X.; Quan, Q.; Liu, G.; Zhang, G.; Choi, K.-Y.; Kim, K.; Sun, X.; Lee, S.; Sun, S.; Leapman, R.; Chen, X. Manipulating the Power of an Additional Phase: A Flower-like Au−Fe_3O_4 Optical Nanosensor for Imaging Protease Expressions In vivo. *ACS Nano*, **2011**, *5*, 3043–3051.

[32] Lee, Y.; Garcia, M.A.; Frey Huls, N.A.; Sun, S. Synthetic Tuning of the Catalytic Properties of Au-Fe3O4 Nanoparticles. *Angew. Chemie Int. Ed.*, **2010**, *49*, 1271–1274.

[33] Carta, D.; Casula, M.F.; Falqui, A.; Loche, D.; Mountjoy, G.; Sangregorio, C.; Corrias, A. A Structural and Magnetic Investigation of the Inversion Degree in Ferrite Nanocrystals MFe_2O_4 (M = Mn, Co, Ni). *J. Phys. Chem. C*, **2009**, *113*, 8606–8615.

[34] Chen, R.; Christiansen, M.G.; Anikeeva, P. Maximizing hysteretic losses in magnetic ferrite nanoparticles via model-driven synthesis and materials optimization. *ACS Nano*, **2013**, *7*, 8990–9000.

[35] Fantechi, E.; Campo, G.; Carta, D.; Corrias, A.; de Julián Fernández, C.; Gatteschi, D.; Innocenti, C.; Pineider, F.; Rugi, F.; Sangregorio, C. Exploring the Effect of Co Doping in Fine Maghemite Nanoparticles. *J. Phys. Chem. C*, **2012**, *116*, 8261–8270.

[36] Fantechi, E.; Innocenti, C.; Albino, M.; Lottini, E.; Sangregorio, C. Influence of cobalt doping on the hyperthermic efficiency of magnetite nanoparticles. *J. Magn. Magn. Mater.*, **2015**, *380*, 365–371.

[37] Schieber, M.M. Iron oxides and their compounds. In *Experimental Magnetochemistry: Nonmetallic Magnetic Materials*; Wohlfarth, E.P., Ed.; North-Holland Publishing Company: Amsterdam, **1967**; p. 158.

[38] Carta, D.; Corrias, A.; Falqui, A.; Brescia, R.; Fantechi, E.; Pineider, F.; Sangregorio, C. EDS, HRTEM/STEM, and X-ray absorption spectroscopy studies of co-substituted maghemite nanoparticles. *J. Phys. Chem. C*, **2013**, *117*, 9496–9506.

[39] Zhou, S.; Han, X.; Fan, H.; Liu, Y. Electrochemical Sensing toward Trace As(III) Based on Mesoporous $MnFe_2O_4$/Au Hybrid Nanospheres Modified Glass Carbon Electrode. *Sensors*, **2016**, *16*, 935.

[40] Silvestri, A.; Mondini, S.; Marelli, M.; Pifferi, V.; Falciola, L.; Ponti, A.; Ferretti, A.M.; Polito, L. Synthesis of Water Dispersible and Catalytically Active Gold-Decorated Cobalt Ferrite Nanoparticles. *Langmuir*, **2016**, *32*, 7117–7126.

[41] Saire-Saire, S.; Barbosa, E.C.M.; Garcia, D.; Andrade, L.H.; Garcia-Segura, S.; Camargo, P.H.C.; Alarcon, H. Green synthesis of Au decorated $CoFe_2O_4$ nanoparticles for catalytic reduction of 4-nitrophenol and dimethylphenylsilane oxidation. *RSC Adv.*, **2019**, *9*, 22116–22123.

[42] Guo, J.-L.; Chiou, Y.-D.; Liang, W.-I.; Liu, H.-J.; Chen, Y.-J.; Kuo, W.-C.; Tsai, C.-Y.; Tsai, K.-A.; Kuo, H.-H.; Hsieh, W.-F.; Juang, J.-Y.; Hsu, Y.-J.; Lin, H.-J.; Chen, C.-T.; Liao, X.-P.; Shi, B.; Chu, Y.-H. Complex Oxide-Noble Metal Conjugated Nanoparticles. *Adv. Mater.*, **2013**, *25*, 2040–2044.

[43] Li, Y.; Zhang, Q.; Nurmikko, A. V.; Sun, S. Enhanced Magnetooptical Response in Dumbbell-like Ag−$CoFe_2O_4$ Nanoparticle Pairs. *Nano Lett.*, **2005**, *5*, 1689–1692.

[44] Jiang, G.; Huang, Y.; Zhang, S.; Zhu, H.; Wu, Z.; Sun, S. Controlled synthesis of Au-Fe heterodimer nanoparticles and their conversion into Au-Fe_3O_4 heterostructured nanoparticles. *Nanoscale*, **2016**, *8*, 17947–17952.

[45] Sun, S.; Zeng, H.; Robinson, D.B.; Raoux, S.; Rice, P.M.; Wang, S.X.; Li, G. Monodisperse MFe_2O_4 (M = Fe, Co, Mn) nanoparticles. *J. Am. Chem. Soc.*, **2004**, *126*, 273–279.

[46] Hiramatsu, H.; Osterloh, F.E. A Simple Large-Scale Synthesis of Nearly Monodisperse Gold and Silver Nanoparticles with Adjustable Sizes and with Exchangeable Surfactants. *Chem. Mater.*, **2004**, *16*, 2509–2511.

[47] Schneider, C.A.; Rasband, W.S.; Eliceiri, K.W. NIH Image to ImageJ: 25 years of image analysis. *Nat. Methods*, **2012**, *9*, 671–675.

[48] Mason, W.R. Spectrometer for simultaneous measurement of absorption and circular dichroism spectra. *Anal. Chem.*, **1982**, *54*, 646–648.

[49] Fantechi, E.; Roca, A.G.; Sepúlveda, B.; Torruella, P.; Estradé, S.; Peiró, F.; Coy, E.; Jurga, S.; Bastús, N.G.; Nogués, J.; Puntes, V. Seeded Growth Synthesis of Au–Fe_3O_4 Heterostructured Nanocrystals: Rational Design and Mechanistic Insights. *Chem. Mater.*, **2017**, *29*, 4022–4035.

[50] Shi, W.; Zeng, H.; Sahoo, Y.; Ohulchanskyy, T.Y.; Ding, Y.; Wang, Z.L.; Swihart, M.; Prasad, P.N. A General Approach to Binary and Ternary Hybrid Nanocrystals. *Nano Lett.*, **2006**, *6*, 875–881.

[51] Yu, H.; Chen, M.; Rice, P.M.; Wang, S.X.; White, R.L.; Sun, S. Dumbbell-like Bifunctional Au−Fe_3O_4 Nanoparticles. *Nano Lett.*, **2005**, *5*, 379–382.

[52] Orbaek, A.W.; Morrow, L.; Maguire-Boyle, S.J.; Barron, A.R. Reagent control over the composition of mixed metal oxide nanoparticles. *J. Exp. Nanosci.*, **2013**, *00*, 1–26.

[53] Bao, N.; Shen, L.; An, W.; Padhan, P.; Heath Turner, C.; Gupta, A. Formation Mechanism and Shape Control of Monodisperse Magnetic $CoFe_2O_4$ Nanocrystals. *Chem. Mater.*, **2009**, *21*, 3458–3468.

[54] Wei, Y.; Klajn, R.; Pinchuk, A.O.; Grzybowski, B.A. Synthesis, Shape Control, and Optical Properties of Hybrid Au/Fe_3O_4 "Nanoflowers." *Small*, **2008**, *4*, 1635–1639.

[55] Schick, I.; Gehrig, D.; Montigny, M.; Balke, B.; Panthöfer, M.; Henkel, A.; Laquai, F.; Tremel, W. Effect of Charge Transfer in Magnetic-Plasmonic Au@MO_x (M = Mn, Fe) Heterodimers on the Kinetics of Nanocrystal Formation. *Chem. Mater.*, **2015**, *27*, 4877–4884.

[56] Zeng, H.; Sun, S. Syntheses, properties, and potential applications of multicomponent magnetic nanoparticles. *Adv. Funct. Mater.*, **2008**, *18*, 391–400.

[57] *Absorption and Scattering of Light by Small Particles*; Bohren, C.F.; Huffman, D.R., Eds.; Wiley-VCH Verlag GmbH: Weinheim, Germany, **1998**.

[58] Kreibig, U.; Vollmer, M. *Optical Properties of Metal Clusters*; Springer-Verlag: Berlin, **1995**.

[59] Wohlfarth, E.P. *Ferromagnetic Materials. A Handbook on the*

Properties of Magnetically Ordered Substances. Volume 2; Wohlfarth, E.P., Ed.; Elsevier, **1980**.

[60] Chen, R.; Christiansen, M.G.; Anikeeva, P. Maximizing Hysteretic Losses in Magnetic Ferrite Nanoparticles via Model-Driven Synthesis and Materials Optimization. *ACS Nano*, **2013**, *7*, 8990–9000.

[61] Del Bianco, L.; Spizzo, F.; Barucca, G.; Ruggiero, M.R.; Geninatti Crich, S.; Forzan, M.; Sieni, E.; Sgarbossa, P. Mechanism of magnetic heating in Mn-doped magnetite nanoparticles and the role of intertwined structural and magnetic properties. *Nanoscale*, **2019**, *11*, 10896–10910.

[62] Campo, G.; Pineider, F.; Bonanni, V.; Albino, M.; Caneschi, A.; De Julián Fernández, C.; Innocenti, C.; Sangregorio, C. Magneto-optical probe for investigation of multiphase fe oxide nanosystems. *Chem. Mater.*, **2015**, *27*, 466–473.

[63] Albino, M.; Fantechi, E.; Innocenti, C.; López-Ortega, A.; Bonanni, V.; Campo, G.; Pineider, F.; Gurioli, M.; Arosio, P.; Orlando, T.; Bertoni, G.; de Julián Fernández, C.; Lascialfari, A.; Sangregorio, C. Role of Zn^{2+} Substitution on the Magnetic, Hyperthermic, and Relaxometric Properties of Cobalt Ferrite Nanoparticles. *J. Phys. Chem. C*, **2019**, *123*, 6148–6157.

[64] Fontijn, W.F.J.; van der Zaag, P.J.; Feiner, L.F.; Metselaar, R.; Devillers, M. a. C. A consistent interpretation of the magneto-optical spectra of spinel type ferrites (invited). *J. Appl. Phys.*, **1999**, *85*, 5100.

[65] Pineider, F.; Campo, G.; Bonanni, V.; de Julián Fernández, C.; Mattei, G.; Caneschi, A.; Gatteschi, D.; Sangregorio, C. Circular Magnetoplasmonic Modes in Gold Nanoparticles. *Nano Lett.*, **2013**, *13*, 4785–4789.

[66] Sepúlveda, B.; González-Díaz, J.B.; García-Martín, A.; Lechuga, L.M.; Armelles, G. Plasmon-Induced Magneto-Optical Activity in Nanosized Gold Disks. *Phys. Rev. Lett.*, **2010**, *104*, 147401.

[67] Zaitoun, M.A.; Mason, W.R.; Lin, C.T. Magnetic Circular Dichroism Spectra for Colloidal Gold Nanoparticles in Xerogels at 5.5 K. *J. Phys. Chem. B*, **2001**, *105*, 6780–6784.

[68] López-Ortega, A.; Takahashi, M.; Maenosono, S.; Vavassori, P. Plasmon induced magneto-optical enhancement in metallic Ag/FeCo core/shell nanoparticles synthesized by colloidal chemistry. *Nanoscale*, **2018**, *10*, 18672–18679.

Electronic Supplementary Material

Modulation of the magnetic properties of gold-spinel ferrite heterostructured nanocrystals

Elvira Fantechi[1](✉), Claudia Innocenti[2,3], Giovanni Bertoni,[4,5] Claudio Sangregorio[2,3], Francesco Pineider[1]

[1] *INSTM and Dept. of Chemistry and Industrial Chemistry, Università di Pisa, Pisa 56124, Italy*
[2] *ICCOM-CNR, Institute for the Chemistry of OrganoMetallic Compounds, Sesto Fiorentino 50019, Italy*
[3] *INSTM and Dept. of Chemistry, Università degli Studi di Firenze, Sesto Fiorentino 50109, Italy*
[4] *IMEM-CNR, Institute of Materials for Electronics and Magnetism, Parma 43124, Italy*
[5] *CNR-NANO, Istituto Nanoscienze, Modena 41125, Italy*

Supporting information to DOI 10.1007/s12274-****-****-* (automatically inserted by the publisher)

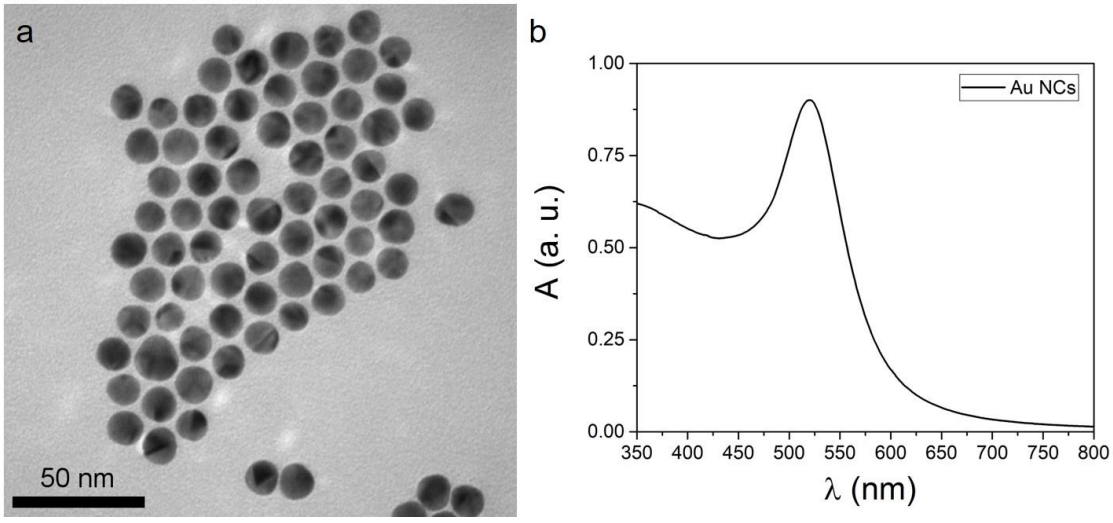

Figure S1 Representative TEM image (a) and extinction spectrum (b) of Au NCs.

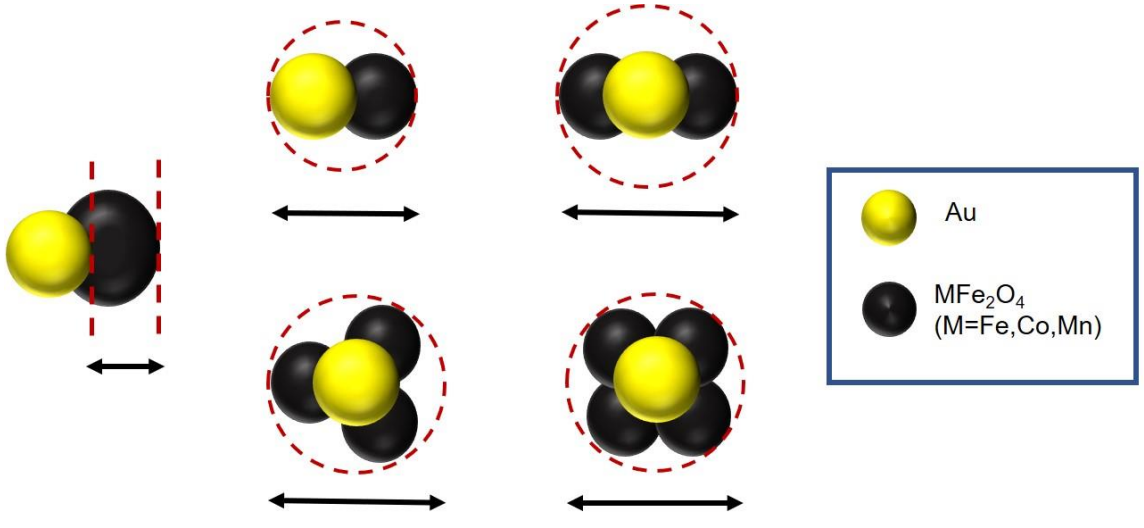

Figure S2 Schematic representation of the evaluation of the total mean size of Au-MFe_2O_4 HNCs and that of the MFe_2O_4 domains. *Black arrow*: distance measured; *dashed red line*: diameter of the circle that circumscribes the HNCs.

Address correspondence to Elvira Fantechi elvira.fantechi@dcci.unipi.it

Table S1 M:Fe ratios (M = Co, Mn) of Au-MFe_2O_4 HNCs obtained from ICP-AES and corresponding spinel ferrite formula.

Sample	Co-ODE	Co-Bz_2O	Mn-ODE	Mn-Bz_2O
Co:Fe	0.75	0.45	-	-
Mn:Fe	-	-	0.21	0.14
x ($M_xFe_{3-x}O_4$)	>1	0.93	0.52	0.38

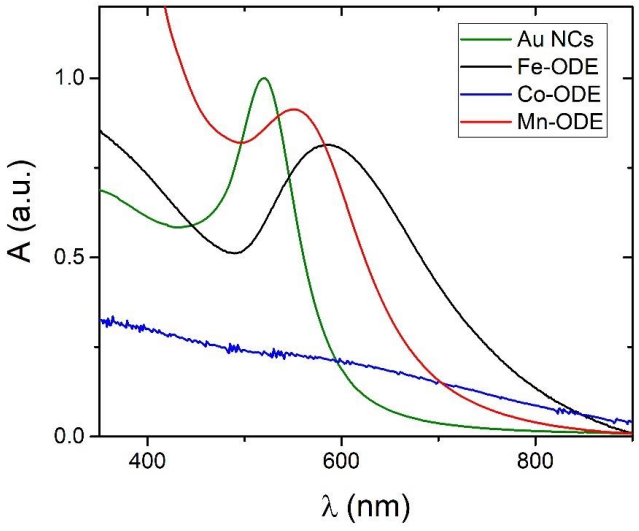

Figure S3 UV−Vis spectra of Au-MFe_2O4 HNCs dispersions in toluene: Fe-ODE (black), Co-ODE (blue) and Mn-ODE (red), together with the Au NCs used as seeds (green).

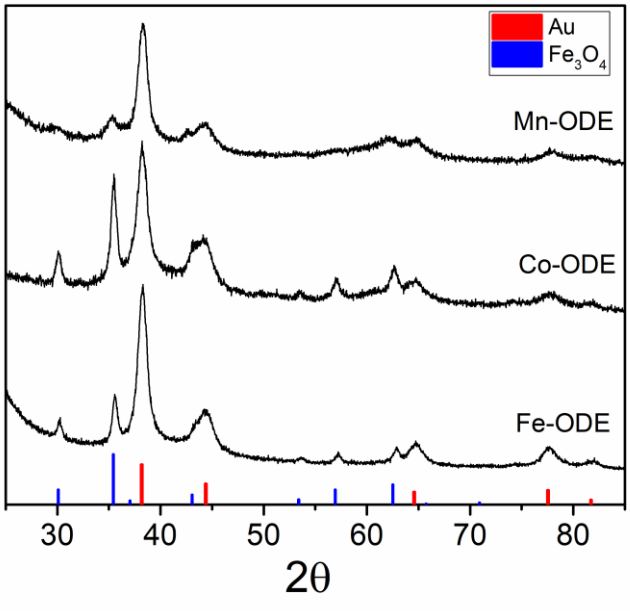

Figure S4 XRD patterns of Au-MFe_2O_4 HNCs, together with the reference patterns of magnetite (PDF 19-0629, blue) and gold (PDF 04-0784, red).

Table S2 Structural and optical properties of Au-MFe_2O_4 HNCs.

	HNCs	MFe_2O_4			Au			HNCs
sample	d_{TEM} (nm)	d_{TEM} (nm)	d_{XRD} (nm)	a (Å)	d_{TEM} (nm)	d_{XRD} (nm)	a (Å)	λ_{max} (nm)
Fe-ODE	23 ± 4	11 ± 3	10.5 (3)	8.370 (2)	13 ± 1	5.57(6)	4.0776 (7)	586
Co-ODE	27 ± 6	10 ± 3	9.7 (2)	8.388(2)	13 ± 3	4.62(7)	4.0781(9)	-
Mn-ODE[a]	24 ± 5	7 ± 2	-	8.426 (3)	11 ± 2	8.5(1.2)	4.0699 (4)	552

d_{TEM}: HNCs average diameter and standard deviation obtained from TEM analysis; a and d_{XRD}: lattice parameter and crystallite mean size obtained from XRD data analysis (errors are reported in brackets), respectively; λ_{max}: wavelength of the plasmonic resonance. The TEM data reported for sample Mn-ODE refer only to the population of HNCs, while the population of isolated $MnFe_2O_4$ was found to have a mean size of 8 ± 3 nm.

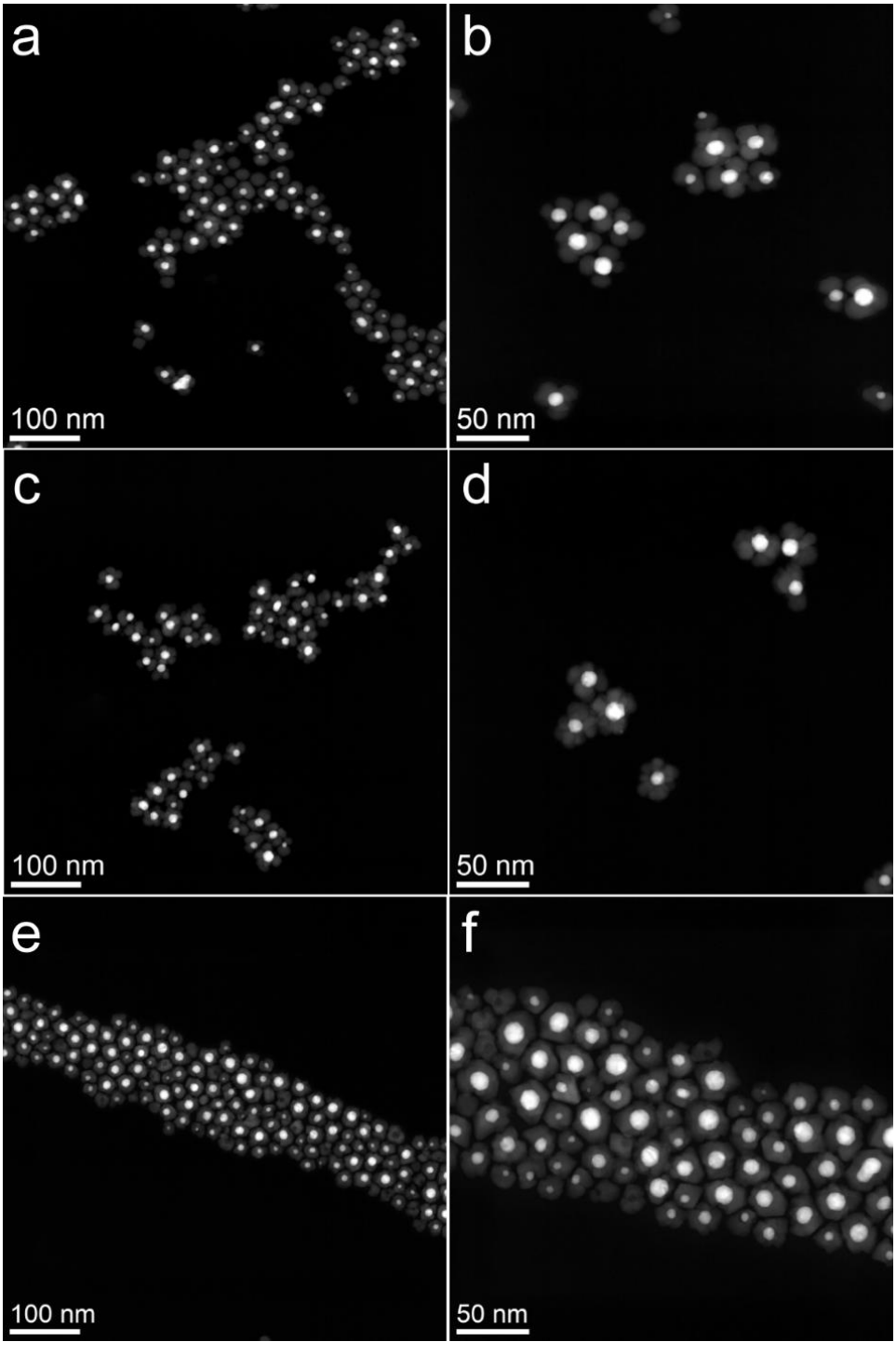

Figure S5 STEM-HAADF images of Au-MFe_2O_4 HNCs samples. a-b) Fe-Bz_2O; c-d) Co-Bz_2O; e-f) Mn- Bz_2O

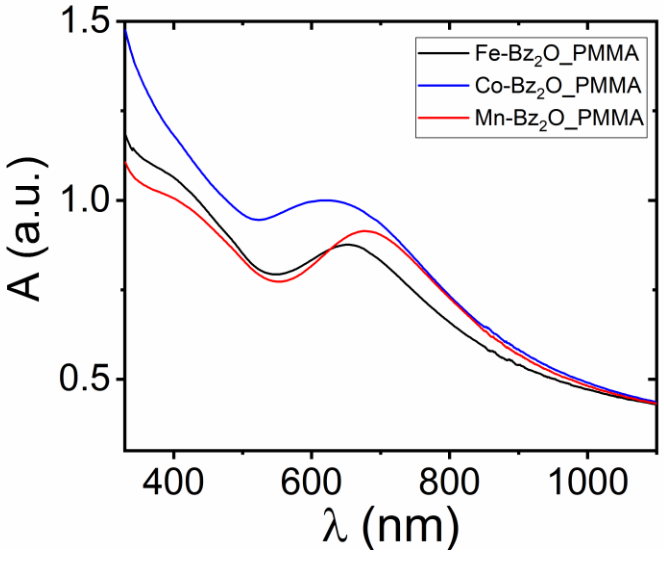

Figure S6 Extinction spectra of Au-MFe_2O_4 HNCs dispersed in PMMA films: Fe-Bz_2O (black), Co- Bz_2O (blue) and Mn- Bz_2O (red).

Fitting of the UV-VIS spectra and simulation of MCD signal from plasmonic component

Each UV-VIS spectrum of Au-MFe_2O_4 HNCs dispersed in PMMA (**Fig. S6**) was fitted as the sum of a Lorentzian peak, arising from LSPR, and a Gaussian peak, approximating high energy interband transitions (**Fig. S7**). The parameters of the Lorentzian line shape (peak amplitude I, peak width γ, ω_0 is the LSPR peak frequency, with $\hbar\omega_0$ the peak energy in eV), were then used to simulate the plasmonic contribution of LSPR to the MCD spectrum as the difference of two Lorentzian peaks shifted by ± half the cyclotron energy with respect to the LSPR energy:

(11~~1~~)

Where $\delta\omega = eB/2m_e$ (B amplitude of the magnetic field, e and m_e electron charge and mass, respectively). The simulated curves are reported in **Fig. S8**, together with the experimental MCD curves.

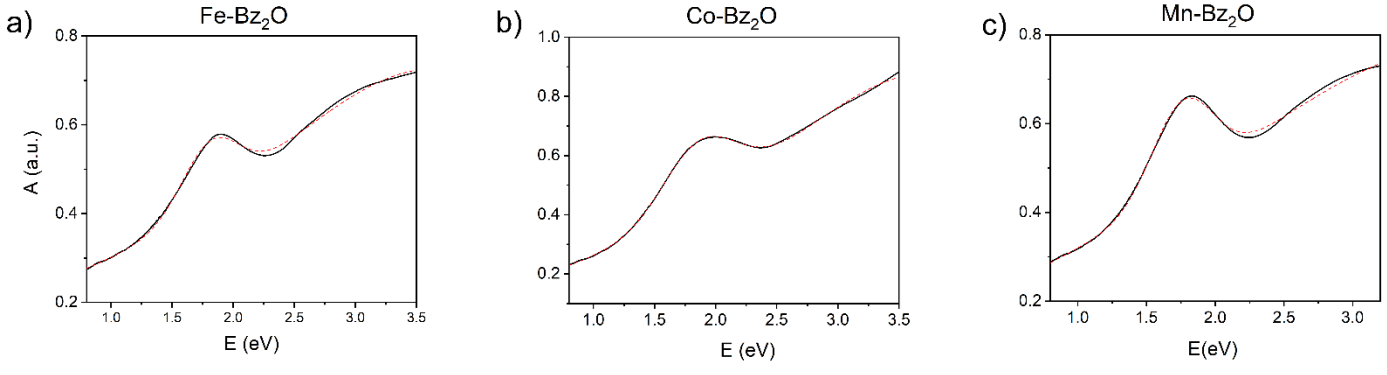

Figure S7 Fit (red dotted line) of UV-Vis spectra (black solid line) of Au-MFe_2O_4 NPs using a combination of a Lorentzian and a Gaussian function.

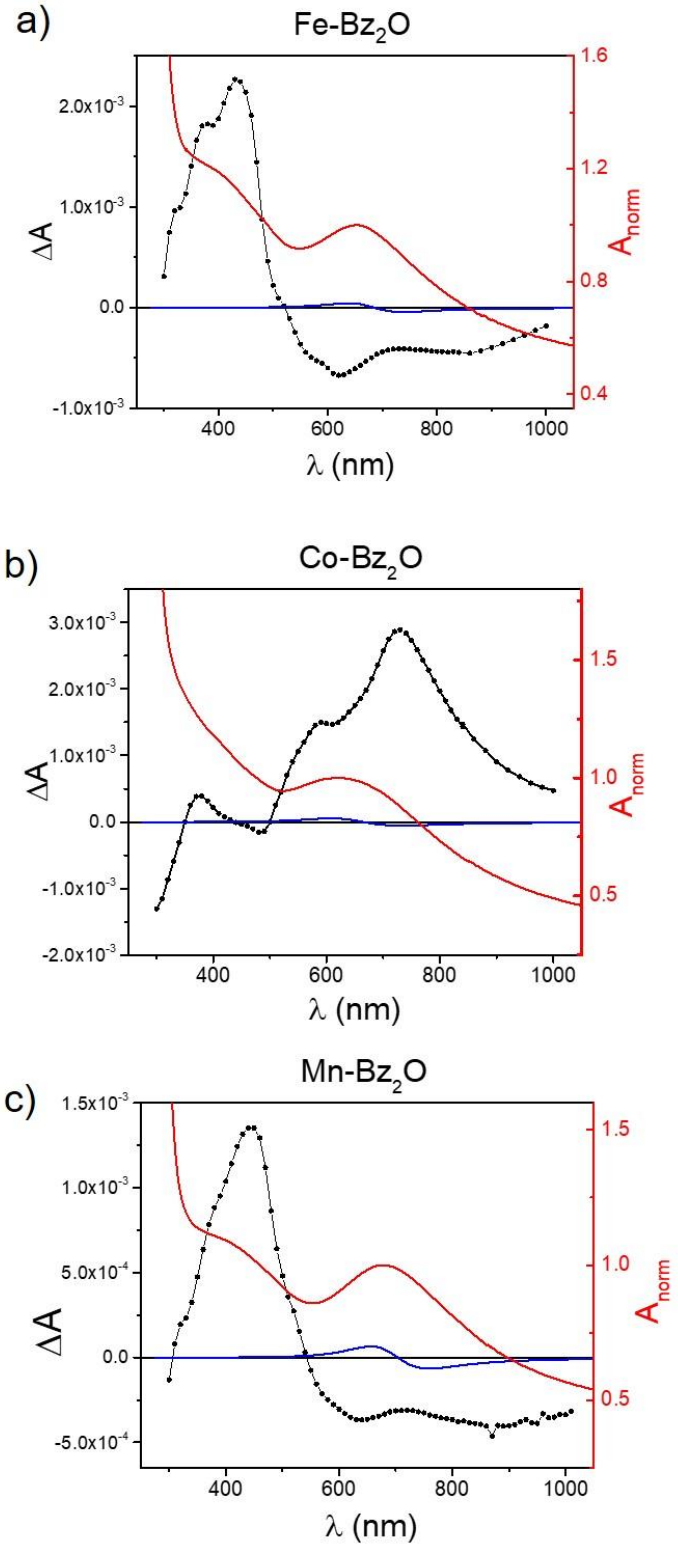

Figure S8 MCD spectra (black) of Au-MFe_2O_4 HNCs in PMMA, compared with the respective UV-VIS spectra (red) and to the simulated MCD signal ascribed to the plasmonic signal only (blue). a) Fe-Bz_2O; b) Co- Bz_2O; c) Mn-Bz_2O.